

The Silicon Vertex Detector of the Belle II Experiment

Y. Uematsu^q, K. Adamczyk^t, L. Aggarwalⁱ, H. Aihara^q, T. Aziz^j, S. Bacher^t, S. Bahinipati^f, G. Batignani^{k,l}, J. Baudot^e, P. K. Behera^g, S. Bettarini^{k,l}, T. Bilka^c, A. Bozek^t, F. Buchsteiner^b, G. Casarosa^{k,l}, L. Corona^{k,l}, T. Czank^p, S. B. Das^h, G. Dujany^e, C. Finck^e, F. Forti^{k,l}, M. Friedl^b, A. Gabrielli^{m,n}, E. Ganiev^{m,n}, B. Gobboⁿ, S. Halder^j, K. Hara^{r,o}, S. Hazra^j, T. Higuchi^p, C. Irmeler^b, A. Ishikawa^{r,o}, H. B. Jeon^s, Y. Jin^{m,n}, C. Joo^p, M. Kaleta^t, A. B. Kaliyar^j, J. Kandra^c, K. H. Kang^s, P. Kapusta^t, P. Kodyš^c, T. Kohriki^r, M. Kumar^h, R. Kumarⁱ, C. La Licata^p, K. Lalwani^h, R. Le Boucher^d, S. C. Lee^s, J. Libby^g, L. Martel^e, L. Massacesi^{k,l}, S. N. Mayekar^j, G. B. Mohanty^j, T. Morii^p, K. R. Nakamura^{r,o}, Z. Natkaniec^t, Y. Onuki^q, W. Ostrowicz^t, A. Paladino^{k,l}, E. Paoloni^{k,l}, H. Park^s, G. Polat^d, K. K. Rao^j, I. Ripp-Baudot^e, G. Rizzo^{k,l}, D. Sahoo^j, C. Schwanda^b, J. Serrano^d, J. Suzuki^r, S. Tanaka^{r,o}, H. Tanigawa^q, R. Thalmeier^b, R. Tiwari^j, T. Tsuboyama^{r,o}, O. Verbycka^t, L. Vitale^{m,n}, K. Wan^q, Z. Wang^q, J. Webb^a, J. Wiechczynski^l, H. Yin^b, L. Zani^d,

(Belle-II SVD Collaboration)

^aSchool of Physics, University of Melbourne, Melbourne, Victoria 3010, Australia

^bInstitute of High Energy Physics, Austrian Academy of Sciences, 1050 Vienna, Austria

^cFaculty of Mathematics and Physics, Charles University, 121 16 Prague, Czech Republic

^dAix Marseille Université, CNRS/IN2P3, CPPM, 13288 Marseille, France

^eIPHC, UMR 7178, Université de Strasbourg, CNRS, 67037 Strasbourg, France

^fIndian Institute of Technology Bhubaneswar, Satya Nagar, India

^gIndian Institute of Technology Madras, Chennai 600036, India

^hMalaviya National Institute of Technology Jaipur, Jaipur 302017, India

ⁱPunjab Agricultural University, Ludhiana 141004, India

^jTata Institute of Fundamental Research, Mumbai 400005, India

^kDipartimento di Fisica, Università di Pisa, I-56127 Pisa, Italy

^lINFN Sezione di Pisa, I-56127 Pisa, Italy

^mDipartimento di Fisica, Università di Trieste, I-34127 Trieste, Italy

ⁿINFN Sezione di Trieste, I-34127 Trieste, Italy

^oThe Graduate University for Advanced Studies (SOKENDAI), Hayama 240-0193, Japan

^pKavli Institute for the Physics and Mathematics of the Universe (WPI), University of Tokyo, Kashiwa 277-8583, Japan

^qDepartment of Physics, University of Tokyo, Tokyo 113-0033, Japan

^rHigh Energy Accelerator Research Organization (KEK), Tsukuba 305-0801, Japan

^sDepartment of Physics, Kyungpook National University, Daegu 41566, Korea

^tH. Niewodniczanski Institute of Nuclear Physics, Krakow 31-342, Poland

Abstract

The Silicon Vertex Detector (SVD) is a part of the vertex detector in the Belle II experiment at the SuperKEKB collider (KEK, Japan). Since the start of data taking in spring 2019, the SVD has been operating stably and reliably with a high signal-to-noise ratio and hit efficiency, achieving good spatial resolution and high track reconstruction efficiency. The hit occupancy, which mostly comes from the beam-related background, is currently about 0.5% in the innermost layer, causing no impact on the SVD performance. In anticipation of the operation at higher luminosity in the next years, two strategies to sustain the tracking performance in future high beam background conditions have been developed and tested on data. One is to reduce the number of signal waveform samples to decrease dead time, data size, and occupancy. The other is to utilize the good hit-time resolution to reject the beam background hits. We also measured the radiation effects on the sensor current, strip noise, and full depletion voltage caused during the first two and a half years of operation. The results show no detrimental effect on the SVD performance.

Keywords: Silicon strip detector, Vertex detector, Tracking detector, Belle II

1. Introduction

The Belle II experiment [1] aims to probe new physics beyond the Standard Model in high-luminosity e^+e^- collisions at the SuperKEKB collider (KEK, Japan) [2]. SuperKEKB consists of the following components: injector LINAC, positron damping ring, and main storage ring with the electron and

positron beamlines. The Belle II detector is located at the interaction point (IP) of the two beamlines. The main collision energy in the center-of-mass system is 10.58 GeV on the $\Upsilon(4S)$ resonance, which enables various physics programs based on the large samples of B mesons, τ leptons, and D mesons. Also, the asymmetric energy of the 7 GeV electron beam and 4 GeV positron beam is adopted for time-dependent CP violation measurements. The target of SuperKEKB is to accumulate an integrated luminosity of 50 ab^{-1} with peak luminosity of about

Email address: uematsu@hep.phys.s.u-tokyo.ac.jp (Y. Uematsu)

16 $6 \times 10^{35} \text{ cm}^{-2}\text{s}^{-1}$. In June 2021, SuperKEKB recorded the 56
 17 world’s highest instantaneous luminosity of $3.1 \times 10^{34} \text{ cm}^{-2}\text{s}^{-1}$. 57
 18 The data accumulated before July 2021 corresponds to an integrated 58
 19 luminosity of 213 fb^{-1} . 59

20 The Vertex Detector (VXD) is the innermost detector in the 60
 21 Belle II detector system. The VXD has six layers: the inner 61
 22 two layers (layers 1 and 2) are the Pixel Detector (PXD), and 62
 23 the outer four layers (layers 3 to 6) are the Silicon Vertex De- 63
 24 tector (SVD). The schematic cross-sectional view of the VXD 64
 25 is shown in Fig. 1. The PXD consists of DEPFET pixel sensors 65
 26 and its innermost radius is 1.4 cm from the IP. A detailed 66
 27 description of the SVD appears in Sec. 2. 67

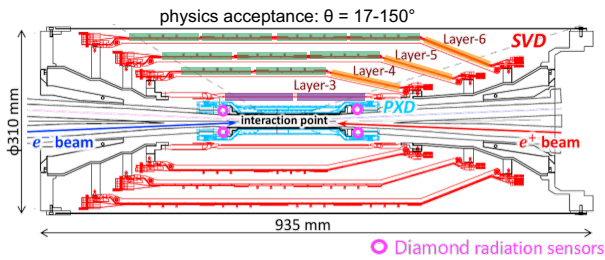


Figure 1: Schematic cross-sectional view of the VXD. The SVD is in red, the PXD in light-blue, and the IP beam pipe diamonds in pink circles. The locations of the three types of DSSDs are indicated by boxes in three colors: purple for small sensors, green for large sensors, and orange for trapezoidal sensors as described in Tab. 1.

28 Besides the VXD, diamond sensors [3] are mounted on the 71
 29 IP beam pipe and the bellows pipes outside of the VXD. The 72
 30 pink circles in Fig. 1 indicate the locations of the diamond 73
 31 sensors on the IP beam pipe. They measure the dose rates in these 74
 32 locations. The measured doses are used to estimate the dose in 75
 33 the SVD. They also send beam abort requests to SuperKEKB 76
 34 if the radiation level gets too high to avoid severe damage to the 77
 35 detector. 78

2. Belle II Silicon Vertex Detector

37 The SVD is crucial for extrapolating the tracks to the PXD. 82
 38 This task is essential for measuring the decay vertices with the 83
 39 PXD and pointing at a region-of-interest limiting the PXD read- 84
 40 out volume. Other roles of the SVD are the standalone track re- 85
 41 construction of low-momentum charged particles and their par- 86
 42 ticle identification using ionization energy deposits. The SVD 87
 43 also plays a critical role in the decay vertex measurement in the 88
 44 case of long-lived particles like K_S mesons, which decay inside 89
 45 the SVD volume. 90

46 The SVD [4] consists of four layers of double-sided silicon 91
 47 strip detectors (DSSDs). The material budget of the SVD is 92
 48 about 0.7% of a radiation length per layer. The aluminum read- 93
 49 out strips are AC-coupled to every other n/p-side strips (elec- 94
 50 trodes) on the n-type substrate over the silicon oxide layer. On 95
 51 each DSSD plane, a local coordinate is defined with u and v : 96
 52 u -axis along n-side strips and v -axis perpendicular to u -axis. 97
 53 In other words, p-side strips and n-side strips provide u and v 98
 54 information, respectively. In the cylindrical coordinate, u corre- 99
 55 sponds to $r-\varphi$ information and v corresponds to z information. 100

The SVD consists of three types of sensors: “small” sensors in layer 3, “large” sensors in the barrel region of layers 4, 5, and 6, and “trapezoidal” sensors in the forward region of layers 4, 5, and 6, which is slanted. They are indicated in blue, green, and orange boxes in Fig. 1. The dimensions for these three types of sensors are summarized in Tab. 1. The sensors are manufactured by two companies: the small and large sensors by Hamamatsu and trapezoidal sensors by Micron. The full depletion voltage is 60 V for Hamamatsu sensors and 20 V for Micron sensors; both types of sensors are operated at 100 V. In total, 172 sensors are assembled, corresponding to a total sensor area of 1.2 m^2 and approximately 224,000 readout strips.

	Small	Large	Trapezoidal
No. of u/p-strips	768	768	768
u/p-strip pitch	$50 \mu\text{m}$	$75 \mu\text{m}$	$50\text{--}75 \mu\text{m}$
No. of v/n-strips	768	512	512
v/n-strip pitch	$160 \mu\text{m}$	$240 \mu\text{m}$	$240 \mu\text{m}$
Thickness	$320 \mu\text{m}$	$300 \mu\text{m}$	$300 \mu\text{m}$
Manufacturer	Hamamatsu		Micron

Table 1: Table of the dimensions for the three types of sensors. Only readout strips are taken into account for number of strips and strip pitch.

The front-end ASIC used in the SVD is APV25 [5], which was originally developed for the CMS silicon tracker. The APV25 is radiation hard for a dose up to 100 Mrad radiation. It has 128 channel inputs and shapers for each channel with a shaping time of about 50 ns. For the SVD, the APV25 is operated in “multi-peak” mode. The mechanism of the data sampling in the multi-peak mode is explained in Fig. 2. The chip samples the height of the signal waveform with the 32 MHz clock (31 ns period) and stores each sample’s information in an analog ring buffer. Since the bunch-crossing frequency is eight times faster than the sampling clock, the stored samples are not synchronous to the beam collision, in contrast to CMS, which motivates operation in the multi-peak mode. In the present readout configuration (the six-samples mode), at every reception of the Belle II global Level-1 trigger, the chip reads out six successive samples of the signal waveform stored in the buffers. The six-samples mode offers enough time window ($6 \times 31 \text{ ns} = 187 \text{ ns}$) to accommodate large timing shifts of the trigger. In preparation for operation with higher luminosity, where background occupancy, trigger dead-time, and the data size increase, we developed the three/six-mixed acquisition mode (mixed-mode). The mixed-mode is a new method to read out the signal samples from the APV25, in which the number of the samples changes between three and six in each event, depending on the timing precision of each Level-1 trigger signal in that event. For triggers with good timing precision, three-samples data are read out and the data have half time window and half data size compared to ones of six-samples data, resulting in the reduction of the effect due to higher luminosity. This functionality was already implemented in the running system and confirmed by a few hours of smooth physics data-taking. Before we start to use the mixed-mode, the effect on the performance due to the change of the acquisition mode is to be

101 assessed. As the first step, the effect in the hit efficiency was
 102 evaluated as described in Sec. 3.

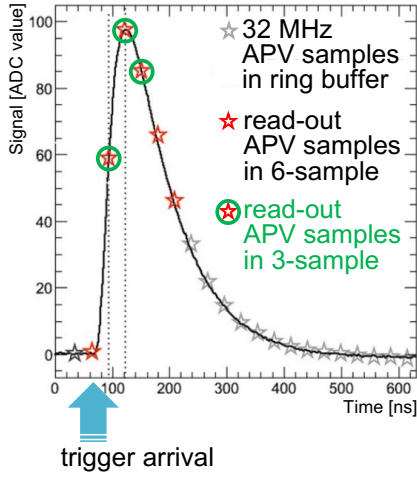


Figure 2: Example of sampling in the “multi-peak” mode of APV25. The black line shows the signal waveform after the CR-RC shaper circuit. The stars show the sampled signal height recorded in the analog ring buffer according to the 32 MHz sampling clock. The red stars indicate the six successive samples read out at the trigger reception in the six-samples mode. The red stars with a green circle indicate the samples read out in the three-samples acquisition.

103 The APV25 chips are mounted on each middle sensor (chip-
 104 on-sensor concept) with thermal isolation foam in between.
 105 The merit of this concept is shorter signal propagation length,
 106 leading to smaller capacitance of the signal line and hence re-
 107 duced noise level. To minimize the material budget the APV25
 108 chips on the sensor are thinned down to 100 μm . APV25s are
 109 mounted on a single side of the sensor and readout of the signals
 110 is from the other side via wrapped flexible printed circuits. The
 111 power consumption of the APV25 chip is 0.4 W/chip and in total
 112 700 W in the entire SVD. The chips are chilled by bi-phase
 113 -20°C CO_2 .

114 3. Performance

115 The SVD was combined with the PXD to complete the VXD
 116 assembly in October 2018, and the VXD was installed to the
 117 Belle II detector system in November 2018. Since March 2019,
 118 the SVD has been operating reliably and smoothly for two and
 119 a half years, without any major problems. The total fraction of
 120 masked strips is about 1%. There was only one issue where one
 121 APV25 chip (out of 1,748 chips) was disabled during the spring
 122 of 2019, which was remediated by reconnecting a cable in the
 123 summer of 2019.

124 The SVD has also demonstrated stable and excellent perfor-
 125 mance [6]. The hit efficiency is continuously over 99% in most
 126 of the sensors. The cluster charge distributions are also reason-
 127 able. On the u/p-side, the most probable values agree with the
 128 calculated charge amount induced by MIPs within the uncer-
 129 tainty in calibration. On the v/n-side, 10–30% of the collected
 130 charge is lost compared to MIP due to the smaller inter-strip
 131 capacitance of the floating strips with larger strip pitches than

the u/p-side. The most probable values of the cluster signal-to-
 132 noise ratio distributions range from 13 to 30.

134 We measured the cluster position resolution by analyzing the
 135 $e^+e^- \rightarrow \mu^+\mu^-$ data [7]. The cluster position resolution is es-
 136 timated from the residual between the cluster position and the
 137 track position not biased by the target cluster after subtracting
 138 the effect of the track extrapolation error. The cluster position
 139 resolutions for different incident angles are shown in Fig. 3. For
 140 normal incident tracks, it agrees with the expectations from the
 141 strip pitch including floating strips. For tracks with an incident
 142 angle, it is expected to get a better resolution, which is indeed
 143 the case in the v/n-side results. However, this effect is not ob-
 144 served on the u/p-side, and the study is still ongoing to improve
 145 the cluster position estimation.

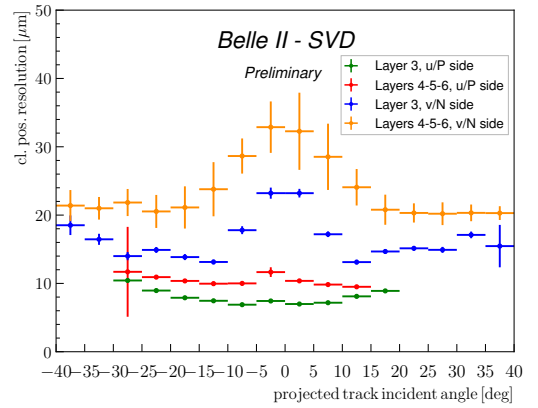


Figure 3: The SVD cluster position resolution depending on the projected track incident angle. The green (blue) plot shows the resolution in the u/p-side (n/v-side) of layer-3 sensors, and the red (yellow) one shows the u/p-side (n/v-side) of layers-4, 5, and 6 sensors.

The cluster hit-time resolution was also evaluated in candi-
 148 date hadronic events¹ using the reference event time estimated
 149 by the Central Drift Chamber (CDC) outside of the SVD. The
 150 error on the event time, about 0.7 ns, was subtracted to evalu-
 151 ate the intrinsic SVD hit-time resolution. The resulting resolu-
 152 tion is 2.9 ns on the u/p-side and 2.4 ns on the v/n-side. With
 153 such precise hit-time information, it is possible to reject off-
 154 time background hits efficiently. The hit-time distributions for
 155 signal² and background³ are shown in Fig. 4. The signal dis-
 156 tribution has a narrow peak, while the background hit-time dis-
 157 tribution is broad and almost flat in the signal peak region. The
 158 separation power of the hit-time is high, as expected. For ex-
 159 ample, if we reject hits with the hit-time less than -38 ns in
 160 this plot, we can reject 45% of the background hits while keep-
 161 ing 99% of the signal hits. The background rejection based on the
 162 hit-time is essential to sustain the good tracking performance in
 163 the future high beam background condition.

The performance in three-samples data was compared with
 164 that in six-samples data to evaluate the performance in the

¹The events with more than three good tracks and not like Bhabha scattering.

²The clusters found to be used in the tracks in the hadronic events.

³The clusters in events triggered by delayed-Bhabha pseudo-random trigger.

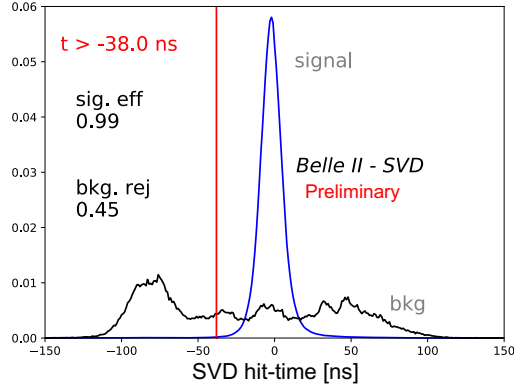


Figure 4: Example of the background hit rejection using hit-time. The blue distribution shows the signal, and the black distribution shows the background. Assuming the hit-time cut at -38 ns, the signal hit efficiency of 99% and the background hit rejection of 45% are achieved.

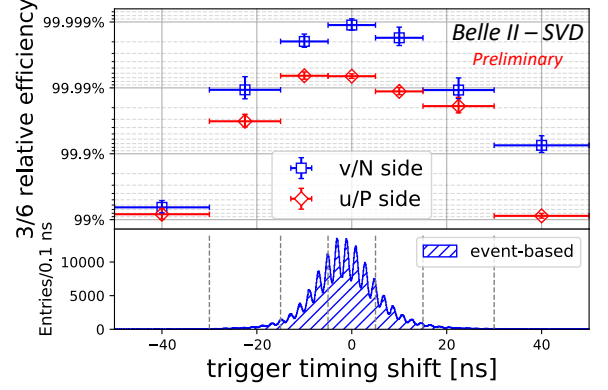


Figure 5: The relative hit efficiencies (the ratios of the hit efficiency in the three-samples data to the one in the six-samples data) as a function of the trigger timing shift for v/n-side (blue square) and u/p-side (red diamond). The positive (negative) trigger timing shift corresponds to early (late) trigger timing.

165 mixed-mode. If the trigger timing has no deviation, the three-²⁰¹
 166 samples data will show comparable performance to the six-²⁰²
 167 samples data because the relevant part of the signal waveform²⁰³
 168 to evaluate the necessary signal properties, which are the signal²⁰⁴
 169 height and the signal timing, can be accommodated in the three-²⁰⁵
 170 sample's time window. However, when the trigger has a jitter²⁰⁶
 171 and the timing shift happens, some part of the signal waveform²⁰⁷
 172 can be out of the three-sample's time window, and the recon-²⁰⁸
 173 struction performance deteriorates. We examined the effect on²⁰⁹
 174 the hit efficiency as a function of the trigger timing shift. The²¹⁰
 175 effect is evaluated by the relative hit efficiency, which is defined²¹¹
 176 as the ratio of the hit efficiency in the three-samples data to the²¹²
 177 one in the six-samples data. For this study, the three-samples²¹³
 178 data are emulated in the offline analysis from the six-samples²¹⁴
 179 data by selecting consecutive three samples at a fixed latency²¹⁵
 180 with respect to the L1 trigger signal. The trigger timing shift²¹⁶
 181 is evaluated by the CDC event time. The resulting relative effi-²¹⁷
 182 ciencies as a function of the trigger timing shift in the hadronic²¹⁸
 183 events are shown in Fig. 5. The decreasing trend is observed for²¹⁹
 184 the shift of the trigger timing, as expected. As a result, the rela-²²⁰
 185 tive efficiency is over 99.9% for the trigger timing shift within²²¹
 186 ± 30 ns, which is almost all the events.

187 4. Beam-related background effects on SVD

188 The beam-related background increases the hit occupancy²²⁶
 189 of the SVD, which in turn degrades the tracking performance.²²⁷
 190 Considering this performance degradation, we set the occu-²²⁸
 191 pancy limit in layer-3 sensors to be about 3%, which will be²²⁹
 192 loosened roughly by a factor of two after we apply the hit-²³⁰
 193 time rejection described in Sec. 3. With the current luminosity,²³¹
 194 the average hit occupancy in layer-3 sensors is less than 0.5%.²³²
 195 However, the projection of the hit occupancy at the luminos-²³³
 196 ity of $8 \times 10^{35} \text{ cm}^{-2}\text{s}^{-1}$ is about 3% in layer-3 sensors. The²³⁴
 197 projected occupancy comes from the Monte Carlo (MC) sim-²³⁵
 198 ulation scaled by the data/MC ratio determined from the beam²³⁶
 199 background data of the current beam optics. The corresponding²³⁷
 200 dose is about 0.2 Mrad/smy, and the equivalent 1-MeV neutron²³⁸

fluence is about $5 \times 10^{11} \text{ n}_{\text{eq}}/\text{cm}^2/\text{smy}$ (smy: Snowmass Year = 10^7 sec). The long-term extrapolation of the beam background is affected by large uncertainties from the optimization of collimator settings in MC and the future evolution of the beam injection background, which is not simulated. This uncertainty motivates the VXD upgrade which improves the tolerance of the hit rates and the radiation damage, and the technology assessment is ongoing for multiple sensor options.

From the measured dose on diamond sensors, the integrated radiation dose in the layer-3 mid-plane sensors, which are the most exposed in the SVD, is estimated to be 70 krad. The estimation is based on the correlation between the SVD occupancy and the diamonds dose. The estimated dose includes uncertainties of about 30% due to the unavailability of the appropriate trigger before December 2020. Assuming the dose/ n_{eq} fluence ratio of $2.3 \times 10^9 \text{ n}_{\text{eq}}/\text{cm}^2/\text{krad}$ from MC, 1-MeV equivalent neutron fluence is evaluated to be about $1.6 \times 10^{11} \text{ n}_{\text{eq}}/\text{cm}^2$ in the first two and a half years.

The effect of the integrated dose on the sensor leakage current is measured, and the results show a clear linear correlation as in the upper plot of Fig. 6. The slopes for all the sensors are summarized in the lower plot of Fig. 6. They are around 2–5 $\mu\text{A}/\text{cm}^2/\text{Mrad}$. The large variations can be explained by temperature effects and the deviation of sensor-by-sensor dose from the average in each layer used in the estimation. The slopes are in the same order of magnitude as previously measured in the BaBar experiment [8], 1 $\mu\text{A}/\text{cm}^2/\text{Mrad}$ at 20°C. While the leakage current is increasing, the impact on the strip noise is suppressed by the short shaping time (50 ns) in APV25. It is expected to be comparable to the strip-capacitive noise only after 10 Mrad irradiation and not problematic for ten years where the integrated dose is estimated to be 2 Mrad.

The relation between the noise and the integrated dose is shown in Fig. 7. The noise increase of 20–25% is observed in layer 3, but this does not affect the SVD performance. This noise increase is likely due to the radiation effects on the sensor surface. Fixed oxide charges on sensor surface increase non-linearly, enlarging inter-strip capacitance. The noise saturation

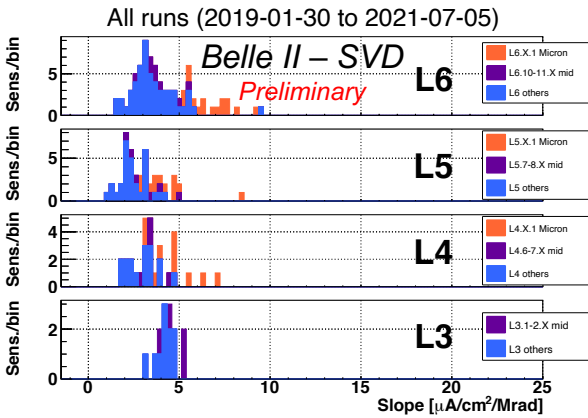
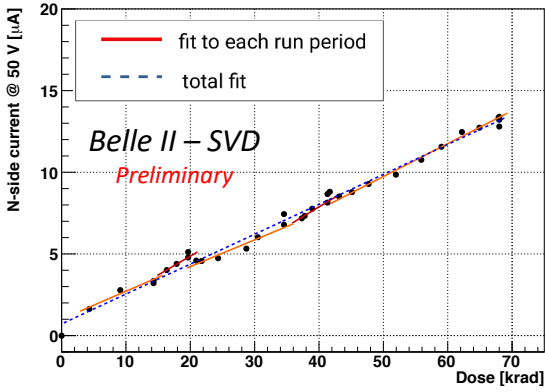


Figure 6: (upper) Effect of the integrated dose on the leakage current in the n/v-side of one layer-3 sensor. The slope is fitted for each run period (solid red line) and for all the runs (dashed blue line). Both fit results agree with each other and are consistent with the linear increase. (lower) The fit results of all the sensors for all runs. The sensors are classified as trapezoidal sensors in the forward region (Micron), sensors around the midplane, and the others.

is observed on the v/n-side and also starts to be seen on the u/p-side. This behavior agrees with the increase of fixed oxide charges.

The full depletion voltage of the sensor is also a key property that can be affected by the radiation damage. It can be measured from the v/n-side strip noise, which suddenly decreases at the full depletion voltage because the sensor substrate is n-type and thus the v/n-side strips can be fully isolated at the full depletion. From this measurement, reasonable full depletion voltages, which are consistent with the values mentioned in Sec. 2, were confirmed, and so far no change in full depletion voltage is observed in the first two and a half years of operation, which is consistent with the expectation from low integrated neutron fluence of $1.6 \times 10^{11} \text{ n}_{\text{eq}}/\text{cm}^2$.

5. Conclusions

The SVD has been taking data in Belle II since March 2019 smoothly and reliably. The detector performance is excellent and agrees with expectations. We are ready to cope with the increased background during higher luminosity running by rejecting the off-time background hits using hit-time and operat-

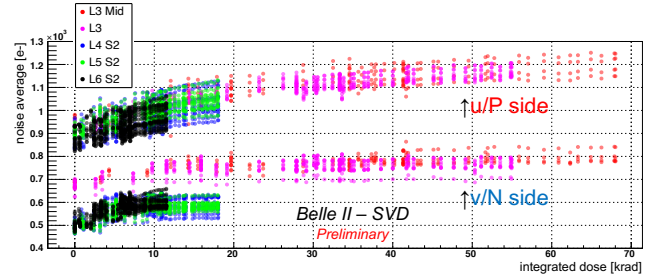


Figure 7: Effect of the integrated dose on the noise average in electron. The clear increase is observed and saturated (or start to be saturated) for layer-3 sensors.

ing in the three/six-mixed acquisition mode. In the recent study, the efficiency loss in the three-samples data is confirmed to be less than 0.1% for the trigger timing shift within $\pm 30 \text{ ns}$. The observed first effects of radiation damage are also within expectation and do not affect the detector performance.

Acknowledgments

This project has received funding from the European Union's Horizon 2020 research and innovation programme under the Marie Skłodowska-Curie grant agreements No 644294 and 822070. This work is supported by MEXT, WPI, and JSPS (Japan); ARC (Australia); BMWFW (Austria); MSMT (Czechia); CNRS/IN2P3 (France); AIDA-2020 (Germany); DAE and DST (India); INFN (Italy); NRF-2016K1A3A7A09005605 and RSRI (Korea); and MNiSW (Poland).

References

- [1] T. Abe, et al., Belle II Technical Design Report (2010). arXiv:1011.0352.
- [2] Y. Ohnishi, et al., Accelerator design at SuperKEKB, Prog. Theor. Exp. Phys. 2013 (3), 03A011 (03 2013).
- [3] S. Bacher, et al., Performance of the diamond-based beam-loss monitor system of Belle II, Nucl. Instrum. Methods Phys. Res., Sect. A 997 (2021) 165157. arXiv:2102.04800.
- [4] K. Adamczyk, et al., The belle ii silicon vertex detector assembly and mechanics, Nucl. Instrum. Methods Phys. Res., Sect. A 845 (2017) 38–42, proceedings of the Vienna Conference on Instrumentation 2016.
- [5] M. J. French, et al., Design and results from the APV25, a deep sub-micron CMOS front-end chip for the CMS tracker, Nucl. Instrum. Methods Phys. Res., Sect. A 466 (2001) 359–365.
- [6] G. Rizzo, et al., The Belle II Silicon Vertex Detector: Performance and Operational Experience in the First Year of Data Taking. arXiv:https://journals.jps.jp/doi/pdf/10.7566/JPSCP.34.010003.
- [7] R. L. Boucher, et al., Measurement of the cluster position resolution of the Belle II Silicon Vertex Detector, these NIMA Conference Proceedings.
- [8] B. Aubert, et al., The BaBar detector: Upgrades, operation and performance, Nucl. Instrum. Methods Phys. Res., Sect. A 729 (2013) 615–701.